The Effects of Turbulence on Metal Nanoparticle Nucleation in Turbulent Jets

A THESIS
SUBMITTED TO THE FACULTY OF THE GRADUATE SCHOOL
OF THE UNIVERSITY OF MINNESOTA
BY

Andrew Jamison Fager

IN PARTIAL FULFILLMENT OF THE REQUIREMENTS
FOR THE DEGREE OF
MASTER OF SCIENCE

Sean C. Garrick

August, 2011

Acknowledgements

First of all I would like to thank my advisor, Professor Sean C. Garrick for his support and guidance during my journey through graduate school at the University of Minnesota. I would like to thank my fellow lab mates: Jun, Nate and Wanjiao who have provided feedback, support and friendship countless times. I would like to thank my family for their unending support and constant encouragement during my education. And finally I thank God for giving me the mental capacity to explore his creation. Any sort of intelligence or creativity in this work is from him.

Abstract

The effects of turbulence on nanoparticle nucleation are studied using a combination of fully resolved and large-scale quantities from direct numerical simulations. A size dependent model for homogeneous nucleation captures the formation of zinc nanoparticles. Growth of these particles is considered by Brownian coagulation. Three simulations are performed using a single Reynolds number and vapor mass-fraction. In one simulation nucleation is computed with fully-resolved data while the remaining two compute nucleation with large-scale filtered data, each at different filter-widths. In all simulations fluid and scalar quantities are fully resolved. A nodal method captures the resultant particle field, approximating the general dynamic equation. Comparisons between the three simulations are made in order to asses the role small-scale turbulent features play on nucleation. Results show that nucleation occurs primarily along the shear layers. Unresolved subgrid-scale nucleation acts to both increase and decrease nucleation. The predominant effect is to decrease nucleation. This leads to an over-prediction of nucleated particles when neglecting the small-scales. The over-prediction is largest in laminar and transitional flow regimes and increases with filter width. No significant discrepancies are seen in the size of nucleated particles when using large-scale quantities.

Contents

List of Tables

List of Figures

Chapter 1

Introduction

Vapor-phase particle formation occurs in a wide variety of processes of engineering and scientific interest. In a number of these processes gas-to-particle conversion via homogeneous nucleation is the dominant mechanism.[1] Additionally, a number of these processes typically occur under turbulent flow conditions. In industrial processes turbulent conditions are often used to rapidly mix quantities important to nucleation, such as temperature and concentration. This increases the saturation which in turn drives the nucleation process. [2, 3, 4] However, our understanding of the role this rapid turbulent mixing has on particle dynamics, including nucleation, is lacking. [1, 3, 4]

It is well known that homogeneous nucleation has a highly non-linear dependence on both temperature and concentration.[5, 6, 1] As a result, fluctuations in these quantities can result in orders of magnitude changes in the local nucleation rate.[7, 8, 9] Simulating nucleation in turbulent flows is both a challenge and a need for many scientific and industrial applications. [4, 3, 10] Methods for simulating turbulent, particle-laden flows fall under three general categories: Direct numerical simulation (DNS), Reynolds-averaged Navier-Stokes simulation (RANS) and large- eddy simulation (LES). DNS solves explicitly for all scales of motion but is computationally prohibitive for all but the simplest flows. RANS simulations have the lowest computation cost, but models all scales of motion. LES falls between RANS and DNS in computational cost. It has the advantage of DNS in that it captures the large-scale dynamics while modeling the small, or subgrid-scale (SGS) dynamics. Recently, both DNS and LES were used to study the formation and growth of titania particles. [11, 12] These simulations showed that the small subgrid

scales act to inhibit more than enhance particle growth. In another study LES was used to investigate binary nucleation in the atmosphere. [9] The results show that large-scale variations in temperature and concentration caused large deviations (up to three orders of magnitude) in the local rate of nucleation. However, this study did not consider the effects of the small- scales on nucleation, as their methodology resolved only the large-scales. Both RANS and LES provide an efficient means to simulate particle laden flows, but they require models for all non-linear interactions. These "turbulence models" have been widely developed and utilized for turbulent reacting flows.[13, 14, 15, 16] However, modeling of the small-scale, unresolved fluctuations on homogeneous nucleation is challenging. Recently, researchers utilized a probability-based method to model the formation of dibutyl-pthalate in round jets. [17] The study showed that the discrepancies between model and the physical data, in the proximal, or near-field, region of jet was greater than in the post-potential-core- collapse region. This is where molecular mixing is the dominant mixing mechanism and the shortcomings of mixing models are exploited.[18] While probability density function methods are quite robust in their accommodation of non-linear terms, their sensitivity to mixing models/closures renders their application to particle nucleation challenging.

In this work we perform simulations of zinc nanoparticle nucleation in turbulent jets. The flows consist of a high-speed jet of zinc metal vapor issuing into a cooler stream. As the two streams mix, the metal vapor becomes super-saturated and nanoparticles form via nucleation (and grow via condensation and coagulation). We utilize DNS and a hybrid DNS-LES approach to assess the effect of the small or unresolved-scale thermochemical fields on the particle nucleation. Spatial filtering of the thermodynamic and species fields is used to obtain the large-scale components. In the DNS all length and time-scales are resolved. This serves as a benchmark simulation. In the hybrid DNS-LES approach a combination of fully- resolved variables and large-scale variables are used to obtain the particle field. More precisely, when computing the nucleation rate and critical diameter the temperature, density, and vapor concentrations are filtered, at two different filter levels, to remove the small-scale features. This approach allows us identify the effects of the small, unresolved scales on nucleation.

Chapter 2

Formulation

2.1 Fluid Transport

The flows under consideration are governed by the compressible Navier-Stokes equations. The primary transport variables are the velocity vector $u_i(\mathbf{x}, t)$, the fluid pressure $p(\mathbf{x}, t)$, the fluid density $\rho(\mathbf{x}, t)$ and the enthalpy $h(\mathbf{x}, t)$, where $\mathbf{x} = (x, y, z)$ denotes the spatial coordinates. These variables are obtained via the conservation of mass, momentum, and enthalpy:

$$\frac{\partial \rho}{\partial t} + \frac{\partial \rho u_j}{\partial x_j} = 0; \tag{2.1}$$

$$\frac{\partial \rho u_i}{\partial t} + \frac{\partial \rho u_i u_j}{\partial x_j} = -\frac{\partial p}{\partial x_i} + \frac{\partial \tau_{ij}}{\partial x_j}; \tag{2.2}$$

$$\frac{\partial \rho h}{\partial t} + \frac{\partial \rho u_j h}{\partial x_j} = \frac{\partial}{\partial x_j}\left(\frac{k}{C_p}\frac{\partial h}{\partial x_j}\right). \tag{2.3}$$

The fluid is Newtonian and τ_{ij} is the stress tensor, k is the thermal conductivity and C_p is the specific heat at constant pressure. The system is closed with the ideal gas equation of state, $p = \rho RT$. The fluid temperature is obtained via $dh = C_p dT$.

2.2 Species Transport

The population of species in the flow consists of a inert carrier gas (argon) and trace amounts of a condensing species (zinc vapor). The transport of all species is given by

$$\frac{\partial \rho Y_i}{\partial t} + \frac{\partial \rho u_j Y_i}{\partial x_j} = \frac{\partial}{\partial x_j}\left(\rho D_i \frac{\partial Y_i}{\partial x_j}\right) + \dot{\omega}_i, \tag{2.4}$$

where Y_i is the mass fraction of species i and D_i is its diffusion coefficient. The source/sink term, $\dot{\omega}_i$, represents the effects of gas-to-particle conversion or nucleation,

$$\dot{\omega}_{Zn} = -\rho_{Zn}\frac{\pi d_p^3}{6} J \tag{2.5}$$

where d_p is the nuclei diameter, ρ_{Zn} is the density of the nuclei/particle, and J is the number nucleation rate (particles/$(m^3 \cdot s)$).

2.3 Particle Transport

The transport of nanoscale particles dispersed in the fluid is governed by the aerosol general dynamic equation (GDE). The GDE describes particle dynamics under the influence of various physical and chemical phenomena and is written in discrete form as a population balance on each cluster or particle size. [1] We adopt a nodal approach to represent the GDE.[19] The GDE is therefore solved as a set of transport equations, one for each bin, $k = 1, 2, ..., N_B$, where N_B is the number of bins. [20, 21, 22, 23, 24, 25] The transport equation for the concentration of particles in bin k, Q_k, is given by

$$\frac{\partial \rho Q_k}{\partial t} + \frac{\partial \rho u_j Q_k}{\partial x_j} = \frac{\partial}{\partial x_j}\left(\rho D_k \frac{\partial Q_k}{\partial x_j}\right) + \dot{\omega}_k, \tag{2.6}$$

where D_k is the particle diffusivity given by

$$D_k = k_B T \frac{C_c}{3\pi\mu d_{p,k}}, \tag{2.7}$$

k_B is the Boltzmann constant, C_c is the Cunningham correction factor, and $d_{p,k}$ is the particle diameter of bin k.[1] The source term $\dot{\omega}_k$ represents the particle formation process by homogeneous nucleation and the particle growth process by Brownian coagulation and is given by

$$\dot{\omega}_k = \dot{\omega}_k^C + \dot{\omega}_k^N, \tag{2.8}$$

where $\dot{\omega}_k^C$ is the source term due to Brownian coagulation and $\dot{\omega}_k^N$ is the source term due to nucleation. The role of Brownian coagulation in turbulent flow has been studied extensively. [25, 26, 19, 11] The coagulation source term is given by

$$\dot{\omega}_k^C = \frac{1}{2}\sum_{i=1}^{N_B}\sum_{j=1}^{N_B}\beta_{ij}\chi_{ijk}Q_iQ_j - \sum_{i=1}^{N_B}\beta_{ik}Q_iQ_k \tag{2.9}$$

The Brownian collision frequency function, β_{ij}, is given by

$$\beta_{ij} = \begin{cases} a_1\left(n_i^{1/D_f} + n_j^{1/D_f}\right)^{D_f}\left(1/n_i + 1/n_j\right)^{1/2}, & D_f < 2 \\ a\left(n_i^{1/D_f} + n_j^{1/D_f}\right)^{2}\left(1/n_i + 1/n_j\right)^{1/2}, & D_f \geq 2 \end{cases} \tag{2.10}$$

where $a = (3v_o/4\pi)^{1/6}(6k_bT/\rho_{Zn})^{1/2}$ and $a_1 = 2^{D_f}a/4.89$. Here, v_o is the primary particle volume, v_i is the volume of a particle in bin i, ρ_{Zn} is the particle density, n_i and n_j are the number of primary particles in bins i and j, respectively, and D_f is the fractal dimension, which is introduced to describe the shape of the agglomerate. [27] Collisions between particles typically results in sizes that fall between bins. To account for this a splitting function is used, which distributes the particle size distribution in a mass conserved manner between bins and is given by

$$\chi_{ijk} = \begin{cases} \frac{v_{k+1}-(v_i+v_j)}{v_{k+1}-v_k} & : \text{ if } \quad v_k \leq v_i + v_j < v_{k+1} \\ \frac{(v_i+v_j)-v_{k-1}}{v_k-v_{k-1}} & : \text{ if } \quad v_{k-1} \leq v_i + v_j < v_k \\ 0 & : \text{ otherwise} \end{cases} \tag{2.11}$$

The nucleation source term as a mass rate is given by

$$\dot{\omega}_k^N = \rho_{Zn}\frac{\pi d_p^3}{6}\Xi_k J. \tag{2.12}$$

To account for the nucleation of particles at different sizes an additional splitting function, Ξ_k, is used which distributes the nucleating size distribution in a mass conserved manner between bins and is given by

$$\Xi_k = \begin{cases} \frac{v_{k+1}-v}{v_{k+1}-v_k} & : \text{ if } \quad v_k \leq v < v_{k+1} \\ \frac{v-v_{k-1}}{v_k-v_{k-1}} & : \text{ if } \quad v_{k-1} \leq v < v_k \\ 0 & : \text{ otherwise} \end{cases} \tag{2.13}$$

2.4 Particle Formation

We utilize a homogeneous nucleation formulation to account for the crystallization of metal particles from the vapor phase. A variety of expressions for the homogenous nucleation of particles have been developed over the years.[28, 5, 1] The nucleation rate expression employed in this study is one that has been used to describe the nucleation of metal nanoparticles.[29, 30] It augments classical nucleation theory by prescribing a size-dependent surface tension, σ, in addition to use of the correction factor given by Reiss *et al* [31]. The resultant expression is given as

$$J = \frac{\rho Y_{Zn}}{\pi m_{Zn} d_p} \sqrt{\frac{3\, ln(S)}{\rho_{Zn} \kappa} \frac{d_p}{d_e}}\ \exp\left(-\frac{\pi d_p^2\, \sigma\left(d_p, T\right)}{3 k_B T} \right), \tag{2.14}$$

where Y_{Zn} is the zinc vapor mass fraction, m_{Zn} is its molecular mass, d_p is the critical or nuclei diameter, given by

$$d_p = \frac{4 v_{Zn} \sigma\left(d_p, T\right)}{k_B T ln(S)}, \tag{2.15}$$

v_{Zn} is the molecular volume, S is the saturation ratio, ρ_{Zn} is the particle density, κ is the isothermal compressibility, d_e is the equimolar diameter related to the critical diameter by Tolman's length, and σ is the surface tension of the nuclei taken to be a function of size. The saturation ratio, S is defined as the ratio of the partial pressure to the saturation pressure of the condensing species and for the zinc/argon mixture in this study is given by

$$S = Y_{Zn}\, p\, \frac{MW_{mix}}{MW_{Zn}} \frac{1}{133.32 \times 10^{\left(8.35 - \frac{6400}{T}\right)}}, \tag{2.16}$$

where MW_{mix} is the molecular weight of the mixture, MW_{Zn} is the molecular weight of the condensing species (zinc).

2.5 Nucleation at the Large and Small Scales

The focus of this study is to elucidate the effects of the unresolved, small scales on particle nucleation in turbulent flows. The separation of the large (resolved) and small (unresolved) scales can be accomplished via averaging or filtering.[32, 33, 34, 35] The spatial filtering operation is given by

$$\langle f(\mathbf{x}, t) \rangle = \int_{-\infty}^{+\infty} f(\mathbf{x}, t) h(\mathbf{x}', \mathbf{x}) d\mathbf{x}' \tag{2.17}$$

where $\mathbf{x}$ defines the spatial coordinates, h denotes the spatial filter function, and $\langle f(\mathbf{x},t)\rangle$ represents the filtered value of the transport variable $f(\mathbf{x},t)$. The fluctuating quantity is then obtained via subtraction, i.e. $f' = f - \langle f\rangle$. The filter function used in this study is a box or top-hat filter and is given by

$$h(\mathbf{x}',\mathbf{x}) = \begin{cases} \frac{1}{\Delta_L} & : \quad \text{if} \quad |\mathbf{x}-\mathbf{x}'| \leq \frac{\Delta_L}{2} \\ 0 & : \quad \text{if} \quad |\mathbf{x}-\mathbf{x}'| > \frac{\Delta_L}{2} \end{cases} \tag{2.18}$$

where Δ_L is the filter width. The top-hat or box filter acts as a low-pass filter passing only the low frequencies corresponding to the large-scale flow features and removing the high frequencies associated with the smaller, more uniform, features of the flow. [35]

To study the role of the small-scale turbulent features on nucleation the small-scales present in the quantities used to compute nucleation are removed via filtering. This results in nucleation based only on the large-scales in the flow with small changes or fluctuations in the quantities being ignored. The nucleation rate expression obtained from large-scale filtered quantities, J^F, is given as

$$J^F = \frac{\langle\rho\rangle\langle Y_{Zn}\rangle}{\pi\, m_{Zn}\, d_p^F}\sqrt{\frac{3\, ln(S_F)}{\rho_{Zn}\kappa}\frac{d_p^F}{d_e^F}}\; exp\left(-\frac{\pi\,(d_p^F)^2\,\sigma\left(d_p^F,\langle T\rangle\right)}{3k_B\langle T\rangle}\right). \tag{2.19}$$

In a similar manner, large-scale filtered quantities are then used in equations 2.15 and 2.16 to obtain critical nuclei diameter, d_p^F and saturation ratio, S^F, based on large-scale quantities for use in the expression for nucleation rate based on large-scale quantities, J^F.

Subgrid-scale (SGS) nucleation rate is then be obtained from nucleation rate based on fully resolved and large-scale quantities via subtraction, $J^{SGS} = J - J^F$. This quantity shows the effect small-scale turbulent features play on nucleation. When nucleation is computed from fully resolved quantities the SGS term is inherently captured. When nucleation is computed from only large-scale filtered quantities the SGS term is neglected ($J^{SGS} = 0$). Knowledge of the SGS contributions are useful when only large-scale (or resolved) quantities are available, such as in a large-eddy simulation (LES), and the small-scale (or unresolved) quantities require modeling. The analysis in this study will show what the effects of neglecting the SGS nucleation rate term are and what the consequences are when no modeling is applied for this term in a LES. Neglecting the modeling of SGS effects in source terms have been applied to similar studies of

both chemically reacting and particle laden flows with some success. [36, 12] It should be noted that development of the fluid and scalar fields are captured as fully resolved quantities using DNS. The large-scale filtered quantities are only used for nucleation calculations.

Chapter 3

Results

3.1 Flow configuration

The flows under consideration consist of three-dimensional round jets of diameter D, with a velocity U_o issuing into a co-flowing stream of velocity U_∞. The velocity ratio is $U_\infty/U_o = 0.4$. The Reynolds number, based on jet diameter D, the velocity U_o, and the viscosity ν, is $Re_D = U_o D/\nu = 3200$. The jet is composed of hot zinc (Zn) vapor diluted in argon (Ar) gas (at $T_o = 1000K$), issuing into a co-flowing stream composed of a cooler argon gas (at $T_\infty = 450K$). Initially the jet contains a zinc vapor mass fraction of $Y_{Zn} = 0.001$ and a argon gas mass fraction of $Y_{Ar} = 0.999$.

3.2 Physical assumptions

In this study the bulk density of zinc, ρ_{Zn}, as a function of temperature is used for the density of nucleated particles. The assumption of nucleated particles being spherical is made, corresponding to a fractal dimension of $D_f = 3$. Clusters or agglomerates of nucleated particles formed by Brownian coagulation are assumed to have a fractal dimension of $D_f = 1.8$. This is shown to be a common fractal dimension for agglomerates formed by coagulation. [37, 27] The assumption of fast nucleation is made, where the time required to achieve a steady state rate of nucleation is less than the time scale of the flow and allows the use of a steady state nucleation rate expression. [17, 38] In this study the surface tension in the nucleation expression is modeled as a function of both

temperature and diameter. Size-dependent surface tension has been studied for many years. Recently Onischuk et. al. (2006) derived an approximate expression for metal nanoparticles that was adopted for this study and given as

$$\sigma(d_p, T) = 0.167 \times 10^{-3}(5430 - T)\, exp(-4 + \frac{8}{2 + \frac{0.896}{d_p} - \frac{0.45}{d_p^2}}), \tag{3.1}$$

for Zinc where σ is in units of N/m, d_p is in units of nm, and T is in units of K. [29] The equimolar diameter, d_e, found in the nucleation rate expression is related to the critical diameter, d_p, by Tolman's length. In this study an approximate analytical expression is used[39] with the expression for zinc given by

$$d_e = d_p - \frac{0.9}{d_p} + 0.896. \tag{3.2}$$

where d_p and d_e are both in units of nm and the constants have been determined from experiments. [29]

Table 3.1: Bins with corresponding particle size

Bin, k	Diameter, d_p (nm)
1	0.45
2	0.49
3	0.67
4	0.90
5	1.14
6	1.43
7	1.81
8	2.27
9	2.87
10	3.61
11	4.55
12	5.73
13	7.22

3.3 Numerical specifications

The computations are performed on a domain size of $16D \times 8D \times 8D$ in the x, y, and z directions respectively. A clustered, structured grid is employed with a resolution of $640 \times 480 \times 480$. Grid clustering is used to resolve the shear layers as the flow evolves in the stream-wise direction. Random perturbations have been added at the inlet to accelerate the development of large-scale structures. The numerical method is a hybrid MacCormack based finite-difference scheme that is second order accurate in space and time.[40, 41] For the nodal approximation of the GDE $k = 13$ bins are used to discretize the particle distribution, table 3.1 shows the particle size corresponding to each bin. Three simulations where performed, a DNS and two filtered DNS simulations. The filtered DNS simulations were performed at two different filter levels in order to elucidate the effect of increasing the filter width on particle nucleation. Filter width's of $\Delta_L = 0.1D$ and $\Delta_L = 0.2D$ where chosen for these simulations, hereafter to be designated by FDNS-1 and FDNS-2 respectively. Filter widths of similar size have been used in previous LES studies.[14, 36, 12] The simulation parameters including resolution, filter width, and equivalent LES resolution based on filter width are given in Table 3.2. Each simulation was performed to a non-dimensional time of roughly $t^\star = U_o t/D = 80$ which corresponds to two passes of the slower co-flow through the domain and required $80,000$ CPU hours for the DNS, $160,000$ CPU-hours for FDNS-1 and 520,000 CPU hours for FDNS-2. Both instantaneous and time-averaged data are presented to make qualitative and quantitative assessments on the effect filtering has on the temporal evolution and spatial structure of the particle field. Time-averaged data is represented with an "overbar."

Table 3.2: Simulation parameters

Simulation ID	DNS Resolution	Filter Width (Δ_L)	LES Resolution
DNS	$640 \times 480 \times 480$	-	-
FDNS-1	$640 \times 480 \times 480$	$0.10D$	$320 \times 160 \times 160$
FDNS-2	$640 \times 480 \times 480$	$0.20D$	$160 \times 80 \times 80$

3.4 Fluid Field

Figure 3.1 shows a visualization of the flow field at one instant in time using the Q-criterion. Also known as the Okubo-Weiss factor, the Q-criterion physically shows regions dominated by shear ($Q > 0$) and solid-body rotations ($Q < 0$). [42, 43, 44, 45, 46] The figure shows an iso-surface of $Q = -0.5$ and therefore region of rotation or vorticity dominated fluid. In the proximal regions of the jet well-ordered rings of vorticity dominated fluid represent laminar flow dominated by molecular mixing. By $x/D = 4$ coherent structures develop from instabilities in the jet. In these regions vortex dynamics such as bending and stretching begin to occur. This leads to faster, convective mixing of the hot jet with the cool co-flow than was seen in laminar regions. By roughly $x/D = 8$ large-scale structures begin to interact with each other leading to smaller and smaller structures and eventually resulting in collapse of the potential core. At this point the flow has "transitioned" and is considered fully turbulent. After collapse of the core small-scale turbulent structures dominate the jet and act to further increase mixing.

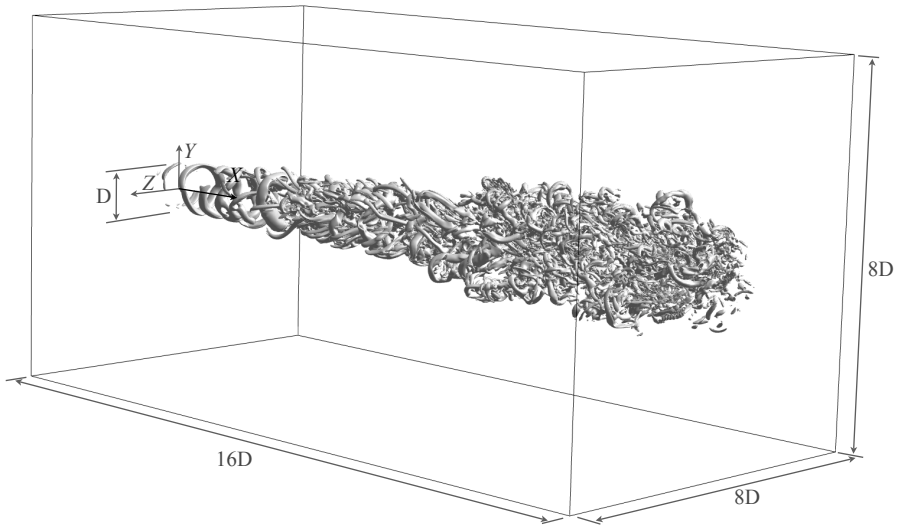

Figure 3.1: Flow configuration, domain size, and instantaneous iso-surface of Q-criterion $Q = -0.5$ at time $t^\star = 80.16$

3.5 Thermal and Species Fields

Instantaneous contours of the fluid temperature, T, are shown in Fig. 3.2. Vertical bars show the sampling locations for the cross stream profiles at $x/D = 1, 5, 10$, and 15. (These downstream locations are used is subsequent figures.) The DNS temperature is shown in Fig. 3.2(a). The image shows that the highest temperatures occur near the inlet of the jet, $x/D = 0$, and persist along the centerline until vortices disrupt the potential core. Conduction is the dominant mode of heat transfer in the proximal region of the jet. As coherent structures appear, convection becomes more significant as large-scale entrainment mixes the hot jet with the cooler co-flow. Beyond $x/D = 8$ the micro-mixing from the small-scale structures cause further cooling of jet as the large-scale gradient set up by convection are reduced through molecular-action/conduction. Contours of the filtered temperatures, $\langle T \rangle_1$, and $\langle T \rangle_2$, from FDNS-1 and FDNS-2, respectively, are shown in Figs. 3.2(b) and 3.2(c). The contours are similar to the DNS temperature except with some small-scale variations removed. These contours were obtained by passing the DNS temperature, T, through a box filter of width $\Delta_L = 0.1D$ for FDNS-1 and $\Delta_L = 0.2D$ for FDNS-2. This has the effect of removing the small-scale fluctuations, or the high wave number content.[47] An example of this is observed between $x/D = 5$ and $x/D = 10$. Comparing the eddies observed in Fig. 3.2(c) with those in 3.2(a) shows that the temperature variation is greatly reduced. So much so that the FDNS-2 temperature, $\langle T \rangle_2$ appears much more "diffuse," as the striation thicknesses observed in Fig. 3.2(c) are greater than those observed in Fig. 3.2(a).[48] The same is observed in Fig. 3.2(b) but to a lesser degree as the filter width is smaller. Filtering may be thought of having the effect of increasing the small-scale mixing but this is not precisely true as it depends on the properties of the filter used.[49, 34]

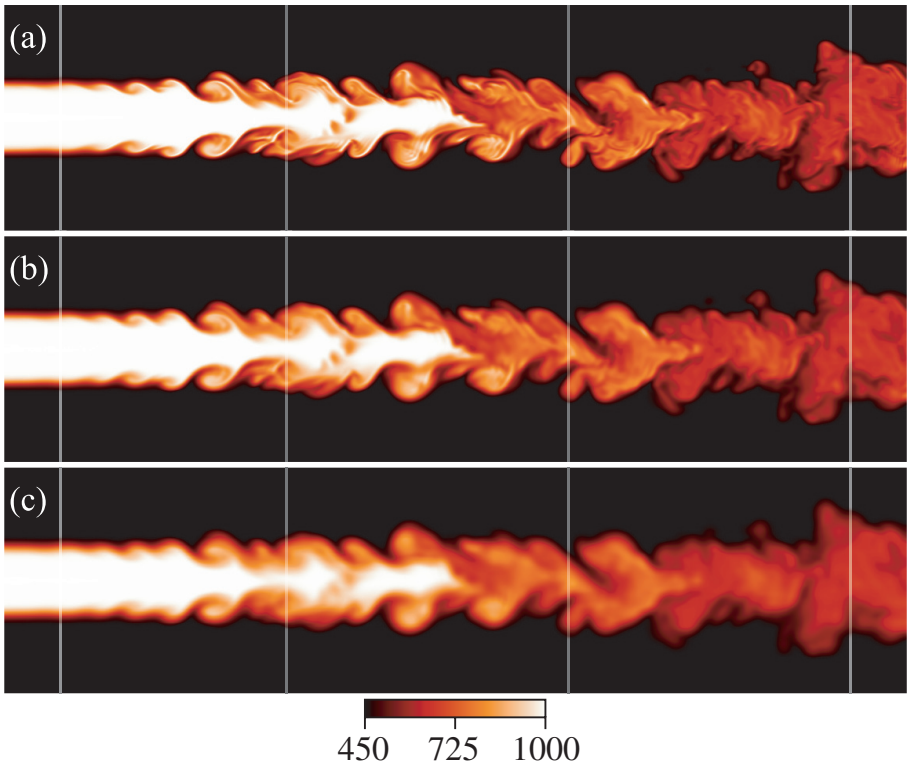

Figure 3.2: Instantaneous contours of temperature, $T(K)$, at time $t^\star = 80.16$ (a) DNS; (b) FDNS-1; (c) FDNS-2. The vertical bars indicate locations $x/D = 1, 5, 10$, and 15, where cross-stream profiles are taken.

To further show the effects of filtering volume rendered visualizations can be seen in Fig. 3.3 showing instantaneous images of both fully resolved and filtered temperature. Part (a) shows the fully resolved or "exact" temperature, T, from the DNS. Part (b) shows the large-scale temperature, $\langle T \rangle_2$, from FDNS-2 Trends seen in the volume rendered temperature field are similar to those seen in Fig. 3.2. Initially mixing is dominated by molecular action in the laminar regions of the jet. Convective mixing of temperature begins to dominate molecular mixing as large-scale coherent structures form. After core collapse small-scale turbulent mixing is seen to dominate near the end of the domain. In the laminar and early transitional regions of the jet no differences between the exact and filtered temperature are seen. However, as structures form difference between exact and filtered temperature appear. Where sharp, prominent structures and strong gradients are present in the exact temperature the filtered temperature contains smoother structures and weaker gradients. After collapse of the jet core the differences become more visible, with many small-scale features present in the exact temperature completely removed in the filtered temperature. These small-scales features, visibly absent in the large-scale temperature, can be especially important when phenomena of interest, such as nucleation or chemistry, have highly non-linear dependencies on temperature and other flow quantities. For example a very common local change or fluctuation in temperature of $T' = 50\ K$ from the large-scale temperature can result in the saturation ratio changing 5-10 fold. Changes this big can then lead to large local changes in nucleation rate.

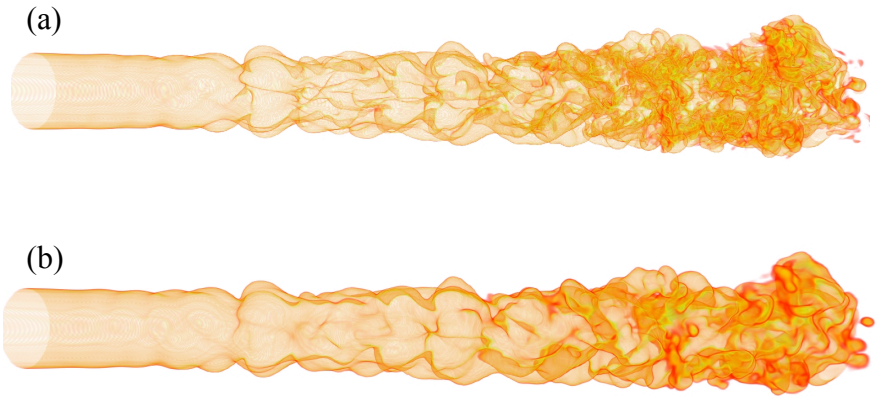

Figure 3.3: Volume rendered image of instantaneous temperature at time $t^\star = 80.16$: (a) fully resolved temperature, T; (b) large-scale filtered temperature, $\langle T \rangle_2$

Cross-stream profiles of the time-averaged non-dimensional temperature, $\overline{\theta} = (\overline{T} - T_\infty)/(T_o - T_\infty)$ and the normalized mass-fraction, $\phi = Y_{Zn}/Y_o$ are shown in Fig. 3.4. At the in-flow plane ($x/D = 0$), the temperature is $\theta = 1$ (or $T = 1000K$). The boiling temperature of zinc is $T = 1180K$. However, because the partial pressure of zinc is 100 Pa while the saturation pressure is 1.2×10^4 Pa, no nucleation occurs. The temperature profiles (Fig. 3.4(a)) show that the jet cools and spreads as it travels down stream. By $x/D = 10$ the jet has cooled to $\overline{\theta} = 0.58$, and by $x/D = 15$, the temperature is $\overline{\theta} = 0.36$ or $\overline{T} = 648K$.

Cross-stream profiles of the time-averaged normalized zinc mass-fraction, $\overline{\phi}$, are shown in Fig. 3.4(b). The profiles are similar to the temperature except for two features. First the mass-fraction profile at $x/D = 1$ is narrower than the temperature profile at the same location. This is a direct result of the temperature boundary condition at $x/D = 0$. This is representative of a physical jet in which the nozzle is heated from the hot metal vapor jet and as a result heats the co-flowing fluid, causing the inlet temperature profile to be wider than the zinc species profile. The other noticeable difference is that the zinc profiles decrease quicker than the temperature profiles. Physically, this means that dilution of the zinc stream (by argon) is greater than cooling of that stream. For example, at $x/D = 10$ the temperature is $\overline{\theta} = 0.58$ and the mass-fraction is $\overline{\phi} = 0.45$, while at $x/D = 15$, the temperature is $\overline{\theta} = 0.36$ and the mass-fraction is $\overline{\phi} = 0.30$. These differences are primarily due to the difference in profiles where the narrower profile means a smaller quantity present in the flow. This quantity is then reduced more readily by turbulent mixing. The non-coincident temperature and mass-fraction profiles results in interesting patterns of cooling and dilution in the flow. Relatively cool regions of the jet still containing zinc vapor are likely to be saturated. For example, under the conditions of $\overline{\theta} = 0.36$ and $\overline{\phi} = 0.30$, the partial pressure of zinc is 30 Pa while the saturation pressure is 4 Pa.

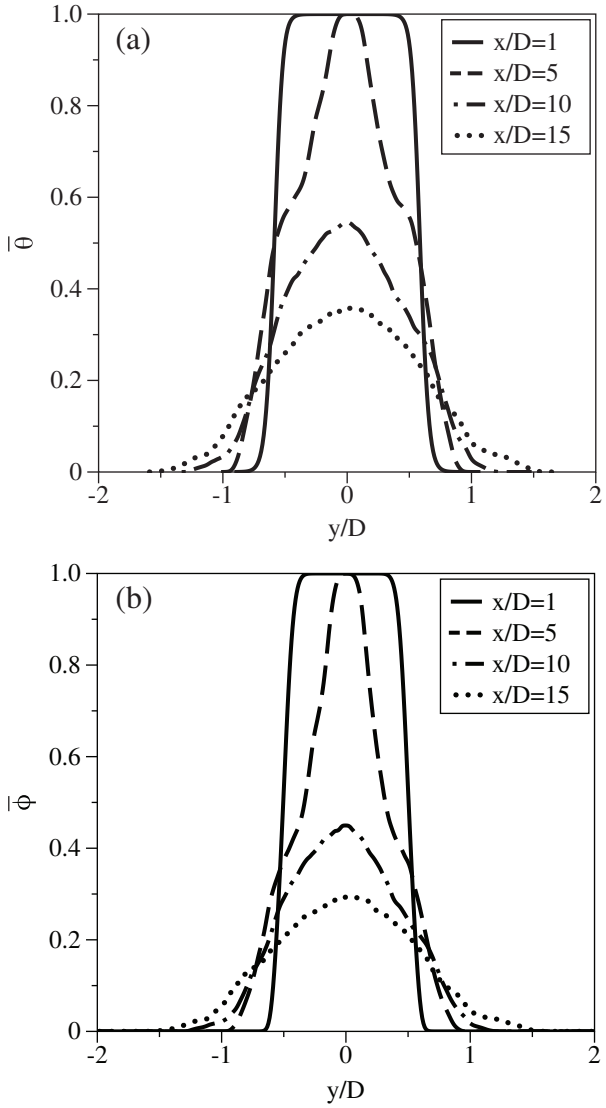

Figure 3.4: Cross-stream profiles of (a) the non-dimensional temperature $\bar{\theta}$ and (b) the normalized zinc vapor concentration $\bar{\phi}$.

3.6 Particle nucleation

3.6.1 Three-Dimensional Visualizations

A visualization of the role temperature on vapor saturation is shown in Fig. 3.5. The figure shows an iso-surface of temperature ($T = 570$) while the log of saturation ratio, $\log_{10} S$, is shown as colors on the iso-surface. The temperature iso-surface shows relatively cool regions of the jet. In the laminar regions of the jet mixing occurs primarily as a molecular scale phenomena through conductive cooling (and diffusive dilution.) This is shown by temperature being very regular and organized initially in the jet. Features appearing as "ripples" begin to develop, showing variations in the temperature field coinciding with large-scale structures forming. These structures lead to regions in the jet where cooling (and dilution) is dominated by convective action with molecular action playing a secondary role. Variations in the temperature field increase further downstream. Small-scale variations become especially prominent after the core collapse. In this region more $T = 570\ K$ regions are visibly present, a result of increased cooling by turbulent mixing. Due to the very low saturation pressure, $P_{sat} = 0.18\ Pa$, at $T = 570\ K$ vapor is expected to become saturated quickly and lead to particle nucleation in these regions. Note: regions of unsaturated vapor, represented by a saturation ratio below unity, $S < 1$, are not shown on the iso-surface. The figure shows that initially vapor is critically saturated if not unsaturated. This is due to the inlet temperature profile being wider than the inlet vapor profile and therefore little to no vapor is initially present at a temperature of $T = 570\ K$. By $x/D = 1$ vapor has begun to diffuse outward from molecular mixing resulting in relatively low levels of vapor saturation. Coherent structures forming around $x/D = 4$ begin to rapidly mix the hot vapor with the cool co-flow, this quickly increases the level of saturation by an order of magnitude in the $T = 570\ K$ regions. As cooling increases in the jet, represented by more $T = 570\ K$ regions in the jet, the level of saturation remains roughly the same. However, more regions of cool vapor results in more regions of saturated vapor. This is especially true after collapse of the core and leads to more sites for particle nucleation.

Visualization of the nucleation particle field is shown in Fig. 3.6 with spherical particles representing nucleation sites in the flow along with iso-surfaces of temperatures at $T = 800\ K$ (red) and $T = 570\ K$. The diameter of the spherical particles in the figure

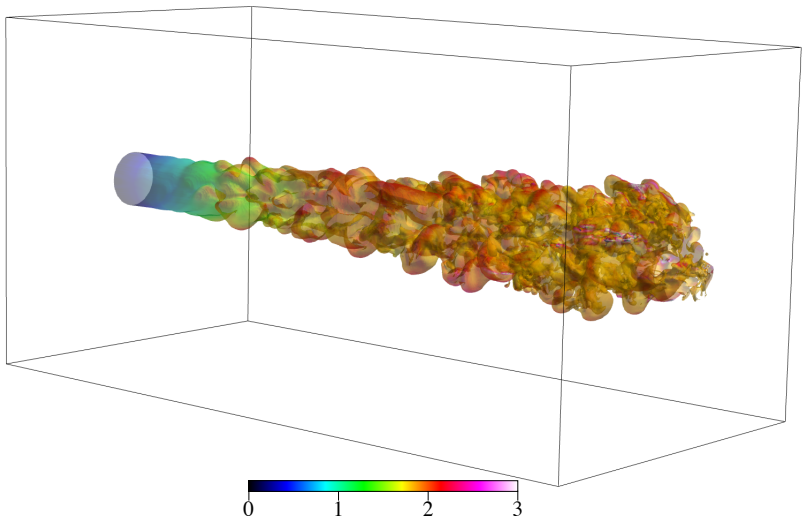

Figure 3.5: Iso-surface of temperature $T = 570\ K$, colors show the log of saturation ratio, $\log_{10} S$, at surface

corresponds to critical diameter of nucleating particles. This images shows qualitatively that the onset of particle nucleation corresponds to the initial development of coherent structures in the jet. As convective mixing in the jet increases the quantity of particles forming also increases. Particles are initially found towards the outer regions of the jet, corresponding to low-temperature (and low vapor saturation) regions. However, after collapse of the core nucleating particles are dispersed in a much more uniform manner across the jet. Inspection of the figure shows that the size of particles nucleating is relatively uniform.

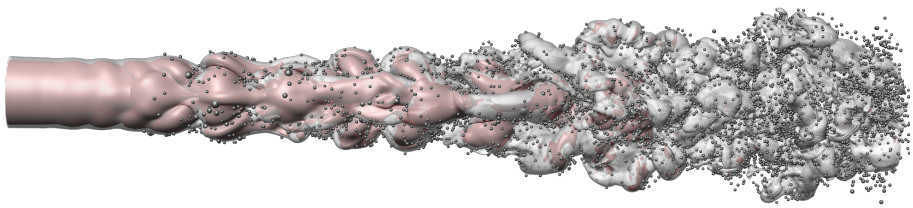

Figure 3.6: Nucleation sites and critical size on iso-surfaces of temperature at time $t^\star = 80.16$. The red iso-surface shows $T = 800\ K$ regions and the gray iso-surface shows $T = 570\ K$ regions.

3.6.2 Saturation ratio

Saturated zinc vapor occurs where the zinc mass-fraction is relatively high and the temperature is relatively low. These combinations yield high partial pressures of zinc vapor, or S, given by Eq. (2.16), greater than unity. Instantaneous contours of the saturation ratio (on the log scale) are shown in Fig. 3.7. The saturation ratio shown in Fig. 3.7(a) is from the DNS data. The contours show that zinc vapor becomes saturated primarily at the interface of the jet and co-flowing streams. The saturation ratio increases and spreads across the width of the jet due to large-scale convective entrainment. Convection sets up large gradients in temperature and mass by which conduction and diffusion then act to decrease, which in turn acts to increase the saturation ratio. At $x/D = 1$ the saturation ratio is quite low - $S < 10$ (note: values below unity, $S < 1$, are not shown due to the log scale). However, as the jet travels downstream the saturation ratio increases to roughly $S = 3900$. Again, the highest values are present at the interface, but Fig. 3.7(a) shows that even near the jet centerline, the values reach as high as $S = 100$. In addition to large-scale and molecular-scale transport, the effects of using the filtered quantities are also present. The saturation ratio obtained from FDNS-1 and FDNS-2 are shown in Fig. 3.7(b) and Fig. 3.7(c), respectively. The contours show that compared to the DNS results, the saturation ratio in the FDNS-1 flow is roughly ten times greater in the proximal region, Ie. $S_1^F > 10S$. In the FDNS-2 flow the difference is even greater. Further downstream, in addition to the aforementioned lack of fine-scale detail, the saturation ratios have similar maximums but, but the maximum value is found over more of the flow-field in the FDNS-1 and FDNS-2 flows.

A more quantitative description is obtained by considering scatter plots of the saturation ratio over the entire flow domain. Instantaneous data is shown in Fig. 3.8. On the x-axis is the DNS saturation ratio, S, and on the y-axis of Fig. 3.8(a) is the FDNS-1 saturation ratio, S_1^F, on the y-axis of Fig. 3.8(b) is the FDNS-2 saturation ratio, S_2^F. Figure 3.8(a) suggests that across the entire domain, when $S = 1$, saturation ratio from filtered quantities is in the range $1 < S_1^F < 4000$, with the majority of points between $S_1^F = 1$ and $S_1^F = 100$. This trend continues for larger saturation ratios, S. For $S = 100$, the data shows the same range of S_1^F values. The difference being a shift in the distribution with the majority of points now found at larger S_1^F values. For the largest saturation ratios, $S > 2000$, S_1^F and S correlate quite well. The trends observed

in the FDNS-2 data are similar. The noticeable difference is that at low values of S, the distribution of S_2^F values is more uniform. Thus, as the filter-width increases, the degree to which the saturation ratio based on the filtered quantities "over-predicts" the true saturation ratio increases.

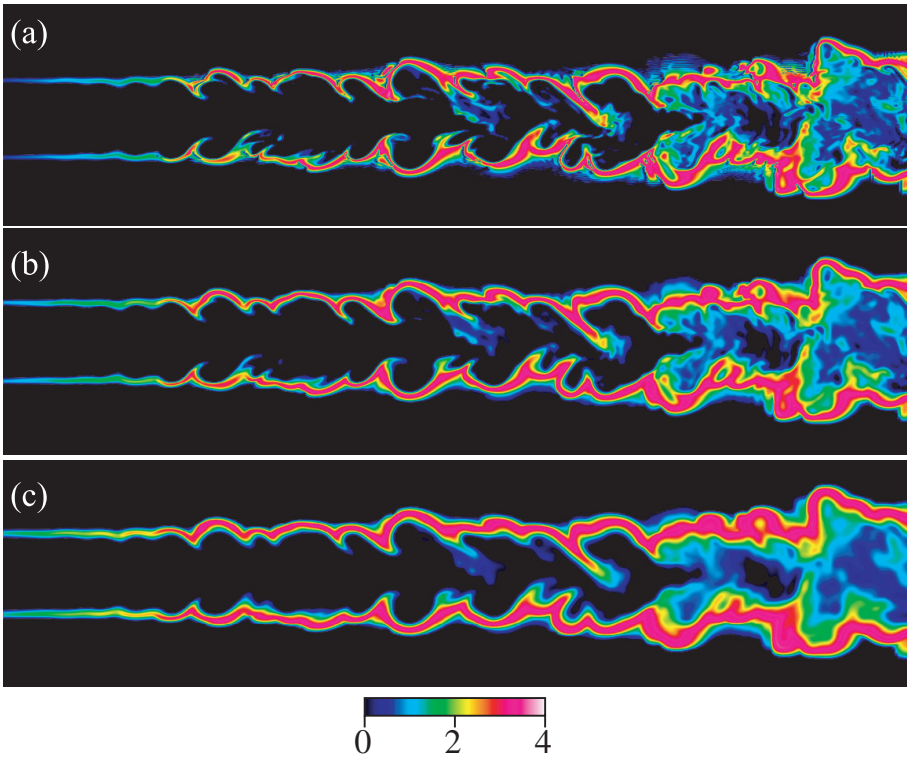

Figure 3.7: Instantaneous contours of saturation ratio, $\log_{10}(S)$, at time $t^\star = 80.16$: (a) DNS; (b) FDNS-1; (c) FDNS-2.

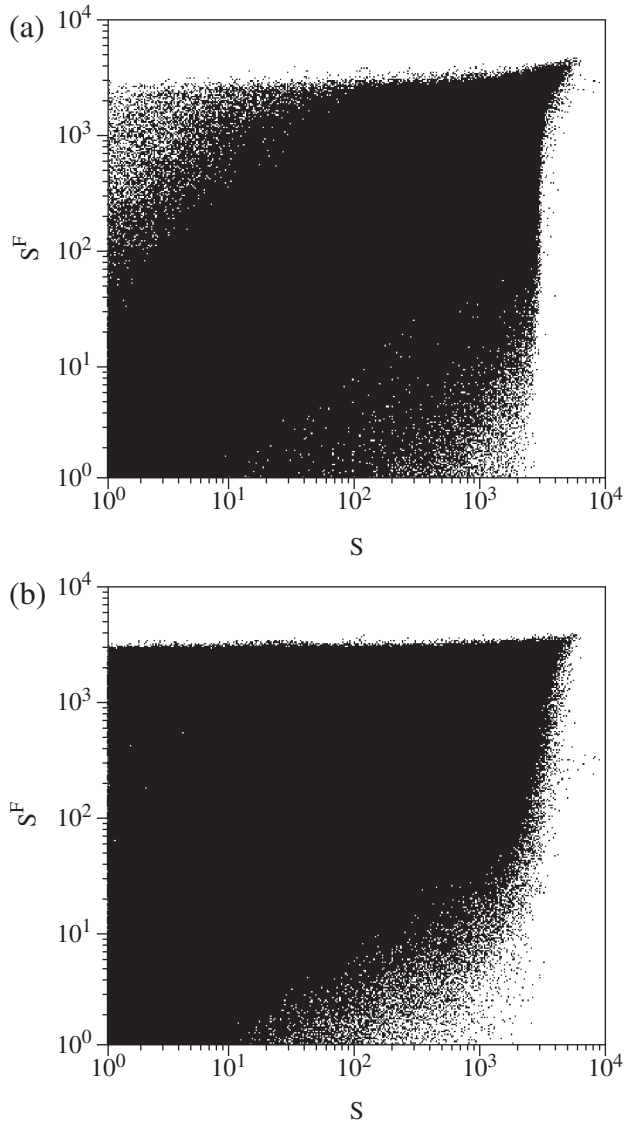

Figure 3.8: Scatter plots of the instantaneous saturation ratio computed from filtered quantities, S_F, vs the exact saturation ratio S at time $t^\star = 80.16$: (a) FDNS-1; (b) FDNS-2.

3.6.3 Nucleation rate

The nucleation rate is an integral quantity for the study of particle formation from the vapor phase. Instantaneous contours of the DNS nucleation rate (on the log scale) are shown in Fig. 3.9(a). The contours show the wide range nucleation rates present in the flow – from $J = 1$ to 10^{19} particles/$(m^3 \cdot s)$. (note: values below unity, $J < 1$, are not shown due to the log scale) It is observed that the combinations of temperature and mass-fraction leading to nucleation primarily occur along the interface of the jet and co-flow. These coincide with regions of high vapor saturation seen in Fig. 3.7. Initially, in the proximal regions of the jet nucleation rate is low around $J = 10^8$ particles/$(m^3 \cdot s)$. However, as large-scale vortical structures begin to form nucleation rate increases many orders of magnitude to $J = 10^{19}$ at the jet/co-flow interface. As small-scale turbulent structures begin to form the areas where nucleation occurs increases. This is due to the generation of smaller and smaller scales, via vortex bending and stretching, which creates more combinations of low-temperature and high-mass-fraction resulting in higher particle nucleation rates.

The rates of particle formation for FDNS-1 and FDNS-2 are shown in Fig. 3.9(b) and Fig. 3.9(c), respectively. The results are similar to the DNS with two noticeable exceptions. First, as the filter width increases, the contours show that nucleation occurs farther upstream, or closer to the jet origin. For example, in the DNS flow, nucleation begins near $x/D = 3$. However, in the FDNS-1 flow, nucleation begins near $x/D = 2$, and, in the FDNS-2 flow, nucleation begins near $x/D = 1$. The second trends is that as the filter width increases the "islands" or pockets of fluid where nucleation occurs disappear. This suggests that without resolving the small-scale activities nucleation bursts may go unobserved or un-counted.

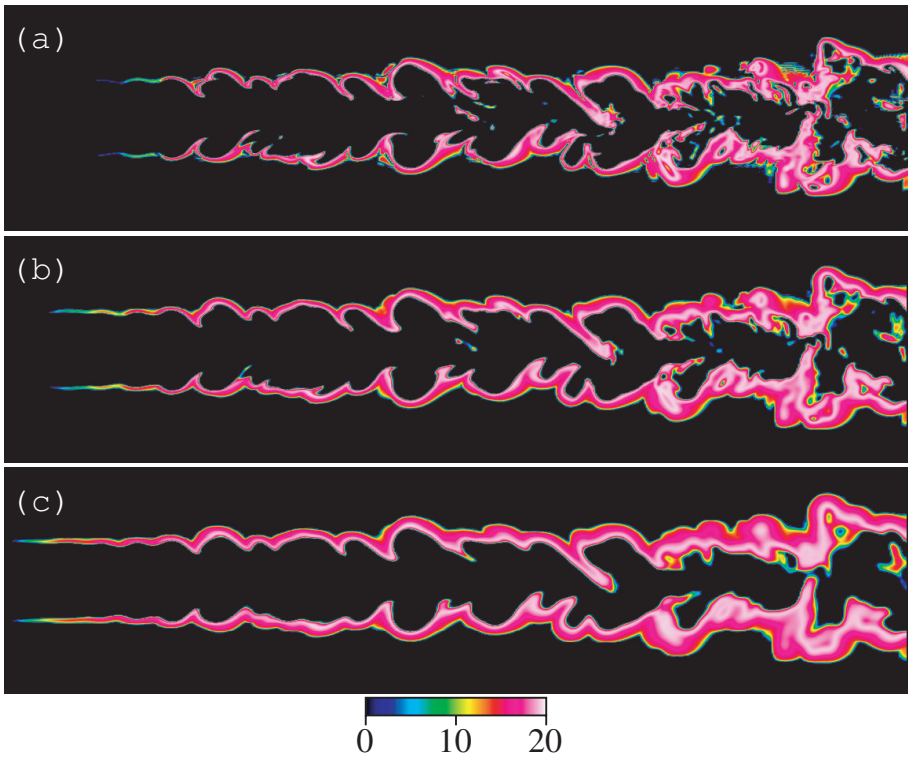

Figure 3.9: Instantaneous contours of nucleation rate, $\log_{10}(J)$ particles/$(m^3 \cdot s)$, at time $t^\star = 80.16$: (a) DNS; (b) FDNS-1 ; (c) FDNS-2.

A probability density function (PDF) of nucleation rate is used to provide a more quantitative view of particle nucleation within the domain. PDFs of the instantaneous nucleation rate are shown in Fig. 3.10. The log of the nucleation rate is used in order to show the wide range of values. In computing all the PDFs for this study points outside of the jet, where $J = 0$ have been removed. Additionally, the x-axis begins at $J = 10^{10}$ for clarity. (The three PDFs are identical below this value.) The curves show bi-modal distributions with peaks near $J = 10^{15}$ and $J = 10^{19}$. It should be noted that the higher peak is four orders of magnitude greater than the lower peak — $J = 10^{19}$ vs $J = 10^{15}$ — and is at least three times more likely. This reflects a tendency for nucleation to be described as an on-off type of phenomena.[1, 9]

Examining the differences between the PDFs of nucleation rate from the DNS, FDNS-1, and FDNS-2 data shows that as the filter width increases, so too does the prominence of each peak. The distribution remains bi-modal but the nucleation rates in the range $10^{15} < J < 10^{19}$ increases. So while the magnitute of the peak rate does not increase, the same nucleation rates occur in a greater extent of the domain. This can also be seen in Fig. 3.9.

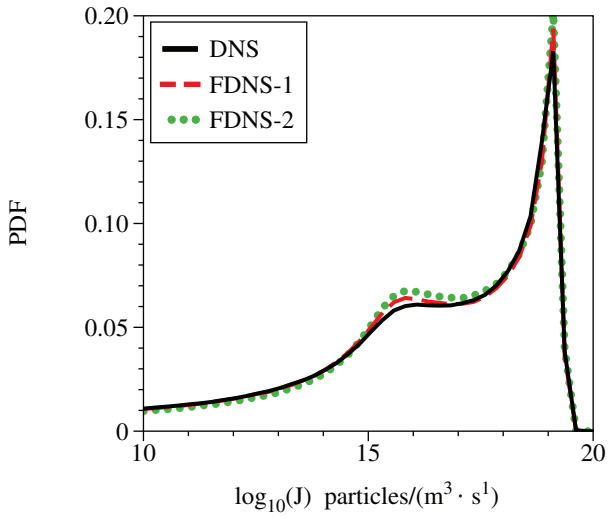

Figure 3.10: Probability density functions of the instantaneous nucleation rates at time $t^\star = 80.16$.

3.6.4 Unresolved or subgrid-scale nucleation rate

We look at the SGS nucleation, J^{SGS}, rate in order to elucidate the effect small, or unresolved scale flow features have on nucleation. A volume rendered image of the SGS nucleation rate J_2^{SGS} computed using the DNS and FDNS-2 data at time $t^\star = 80.16$, is shown in Fig. 3.11. The quantity is decomposed into positive and negative contributions to aid in presentation quality. The green region represents values of $J_2^{SGS} = 10^{19}$ particles/$(m^3 \cdot s)$ and the red regions represents values of $J_2^{SGS} = -10^{19}$ particles/$(m^3 \cdot s)$. Qualitatively, the figure shows that the SGS nucleation is primarily negative in the outer regions of the jet (farther from the jet-centerline) where strong gradients exist along the jet/co-flow interface. Negative SGS nucleation begins to appear near $x/D = 4$, upstream of the potential core collapse, while the positive SGS nucleation values appear in significant quantities farther downstream, after collapse of the jet potential core.

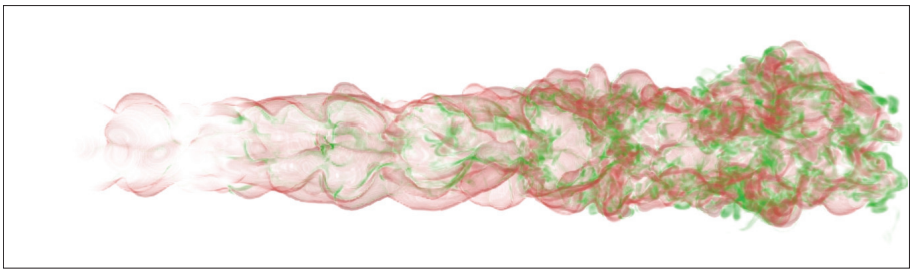

Figure 3.11: Volume rendered image of the subgrid-scale nucleation rate, J_2^{SGS}, from the FDNS-2 quantity at time $t^\star = 80.16$. The red corresponds to regions where $J^{SGS} = -10^{19}$ particles/$(m^3 \cdot s)$, while the green corresponds to regions where $J^{SGS} = 10^{19}$ particles/$(m^3 \cdot s)$.

SGS nucleation is further investigated by focusing separately different regions of the jet in Fig. 3.12. The figure shows contours of SGS nucleation along with an iso-surface of the Q-criterion, $Q = -0.5$, at one instant in time for three different regions of the jet. Blue contours show negative SGS nucleation rates while the yellow contours show positive rates. Figure 3.12(a) shows the laminar regions up to the development of the first coherent structures in the jet ($1 < x/D < 4$). The contours show SGS nucleation is primarily negative ($J^{SGS} < 0$), occurring only on outer regions of the jet as the first coherent structures form. Therefore the small-scales contributions in this area only

act to decrease or inhibit particle nucleation. Figure 3.12(b) shows SGS nucleation in the regions dominated by large-scale convective mixing ($5 < x/D < 8$.) The small-scale activity still occurs in the outer regions of the jet where vapor is relatively cool and likely to be saturated. Negative values occur further away from the jet centerline while the positive values appear closer to the centerline. The figure shows that small-scale activity acts to both increase and decrease nucleation. The negative values acting to decrease nucleation appear to be more prevalent. Figure 3.12(c) shows the fully turbulent regions of the jet dominated by small-scale mixing ($11 < x/D < 14$.) Small-scale or SGS nucleation is seen to be less structured and no longer confined to the outer regions of the jet. In addition SGS nucleation rates are more prevalent across the jet. In these regions the small-scales can be seen to both inhibit and enhance nucleation, with the net effect being unclear in this figure. The SGS nucleation rates are roughly the same order as the actual nucleation rates shown in Fig. 3.6. This points to the strong effect or importance the small-scales play in turbulent nucleation. Again suggesting that fluctuations in quantities important to nucleation can effectively turn on or off local particle nucleation in a turbulent flow.

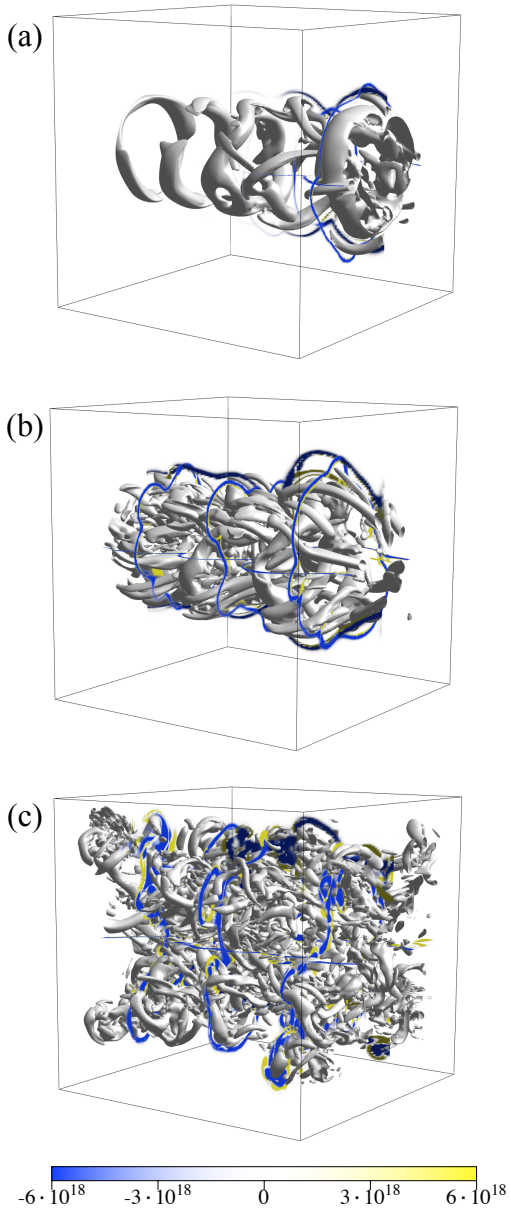

Figure 3.12: Instantaneous contours of subgrid-scale nucleation rate, J^{SGS}, and a iso-surface of Q-criterion $Q = -0.5$ at time $t^\star = 80.16$: (a) $1 < x/D < 4$; (b) $5 < x/D < 8$; (c) $11 < x/D < 14$

A more quantitative view is obtained by constructing PDFs of the negative and positive values as a function of downstream location. The domain is separated into four segments, each four diameters wide, and the resultant PDFs are shown in Fig. 3.13. The negative SGS nucleation rate values ($J^{SGS} < 0$) are shown in Fig. 3.13(a), and positive SGS nucleation rate values ($J^{SGS} > 0$) are shown in Fig. 3.13(b). Note: The x-axis is the log of the absolute value of the SGS nucleation rate. Figure 3.13(a) shows that as flow travels downstream the distribution of negative values becomes bi-modal and more prominent. The SGS nucleation shows peaks at $J^{SGS} = -10^{15}$ and $J^{SGS} = -10^{19}$, and the prominence of these peaks increases with downstream distance. Figure 3.13(b) shows that the positive SGS nucleation values ($J^{SGS} > 0$) has a unimodal distribution with a peak near $J^{SGS} = 10^{19}$. Again, the prominence increases with downstream distance but, generally, they are not as prominent as the negative contributions. For example, in the region $8 < x/D \leq 12$, the probability that $J^{SGS} = +10^{19}$ is almost twice that of $J^{SGS} = -10^{19}$. This suggests that while the unresolved scales act to both increase and decrease nanoparticle nucleation, the tendency to decrease nucleation is greater.

PDFs of the SGS nucleation rate conditioned on normalized zinc mass-fraction fluctuations, $\phi' = \phi - \langle\phi\rangle$, are shown in Fig. 3.14. A positive fluctuation, $\phi' > 0$, means that the fully resolved mass-fraction is larger than the large-scale mass-fraction and physically represents small-scale features concentrating zinc vapor in the flow. In the same way a negative fluctuation, $0 < \phi'$, represents small- scale features diluting zinc vapor in the flow. Negative SGS nucleation rate values ($J^{SGS} < 0$) are shown in Fig. 3.14 (a) and positive SGS nucleation rate values ($J^{SGS} > 0$) are shown in Fig. 3.14(b). Figure 3.14(a) shows that for regions of small-scale dilution the distribution of negative SGS nucleation rate values is bi-modal with peaks at $J^{SGS} = -10^{15}$ and $J^{SGS} = -10^{19}$. For small-scale concentration the distribution is unimodal with a single peak at roughly $J^{SGS} = -10^{19}$. This figure shows that negative SGS nucleation rate values predominately occur in regions of small-scale dilution. Figure 3.14(b) shows for regions of both small-scale concentration and dilution in the flow the distribution of positive SGS nucleation rate values is unimodal with a single peak at $J^{SGS} = 10^{19}$. Similar to panel (a), panel (b) shows that positive SGS nucleation rate values predominately occur in regions of small-scale dilution. Comparison between panel (a) and panel (b) shows that

regions of small-scale dilution contain both positive and negative SGS nucleation rate values, however, the negative values are more predominant. For regions of small-scale concentration there is roughly an equal contribution to negative and positive SGS nucleation values. This suggests that small-scale dilution acts to decrease nucleation more than increase it while small-scale concentration has little to no net effect on nucleation. Small-scale dilution occurs, among other places, along the jet/co-flow interface where filtering smooths gradients and artificially injects vapor into the co-flow, creating negative mass-fraction fluctuations. The increased presence of vapor, from filtering, along the outer regions of the jet in FDNS-1 and FDNS-2 causes more nucleation to occur in these regions for FDNS-1 and FDNS-2. This results in negative SGS nucleation rates in the outer regions of the jet (visible in Fig. 3.11).

PDFs of the SGS nucleation rate conditioned on non-dimensional temperature fluctuations, $\theta' = \theta - \langle\theta\rangle$, are shown in Fig. 3.15. A positive fluctuation, $\theta' > 0$, means that the fully resolved temperature is larger than the large-scale temperature and physically represents small-scale features heating the flow. In the same way a negative fluctuation, $0 < \theta'$, represents small-scale features cooling the flow. The negative SGS nucleation rate values ($J^{SGS} < 0$) are shown in Fig. 3.15(a) and positive SGS nucleation rate values ($J^{SGS} > 0$) are shown in Fig. 3.15(b). The trends seen in the PDFs based on temperature fluctuations in Fig. 3.15 are very similar to those seen for the PDFs based on mass-fraction fluctuations in Fig. 3.14. This suggests two things: (1) that small-scale cooling acts to decrease nucleation more than increase it while small-scale heating has little to no net effect on nucleation and (2) that mass-fraction and temperature fluctuations are likely coincident with each other in the flow. Finally, comparison of the observed trends in Fig. 3.14 and 3.15 suggest that the effect of small-scale dilution reducing the quantity of vapor and thus the nucleation rate dominates the effect of small-scale cooling increasing nucleation by decreasing the saturation pressure.

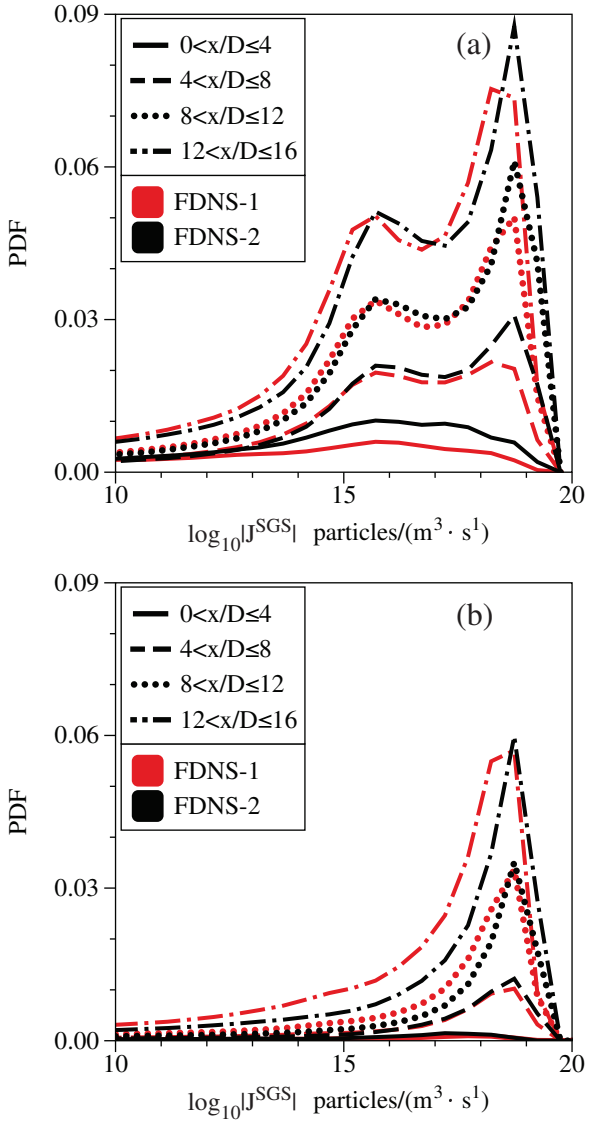

Figure 3.13: Probability density function of subgrid-scale nucleation rate magnitude, $|J^{SGS}|$ conditioned on downstream location at time $t^\star = 80.16$. The red shows $|J_1^{SGS}|$ from the FDNS-1 quantity, while the black shows $|J_2^{SGS}|$ from the FDNS-2 quantity. Panel (a) shows the negative values ($J^{SGS} < 0$) and panel (b) shows the positive values ($J^{SGS} > 0$).

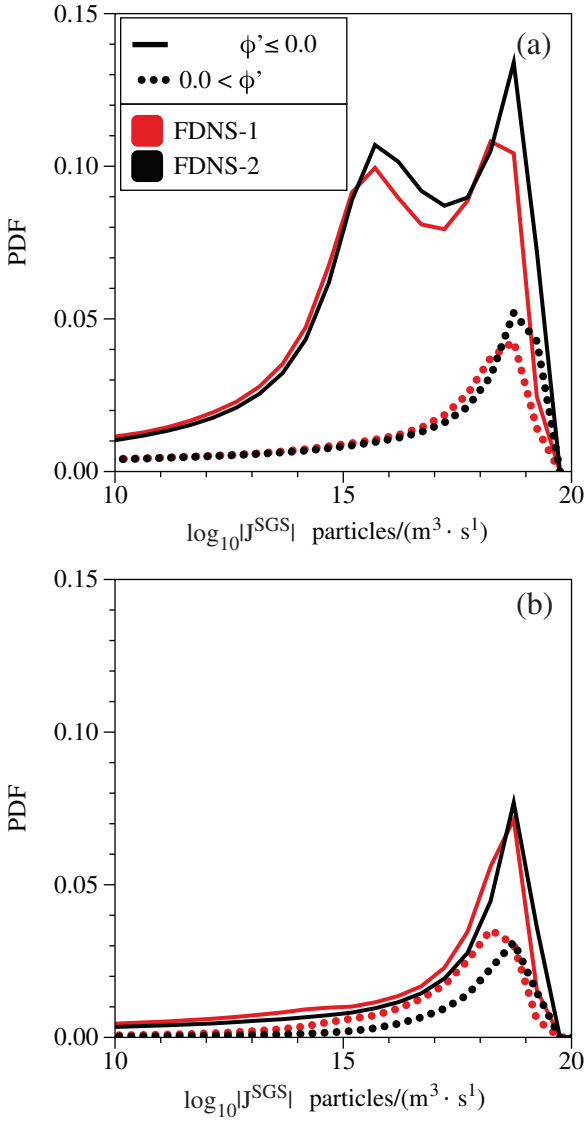

Figure 3.14: Probability density function of subgrid-scale nucleation rate magnitude $|J^{SGS}|$ conditioned on the zinc concentration fluctuation ϕ' at time $t^\star = 80.16$. The red shows $|J_1^{SGS}|$ from the FDNS-1 quantity, while the black shows $|J_2^{SGS}|$ from the FDNS-2 quantity. Panel (a) shows the negative values ($J^{SGS} < 0$) and panel (b) shows the positive values ($J^{SGS} > 0$).

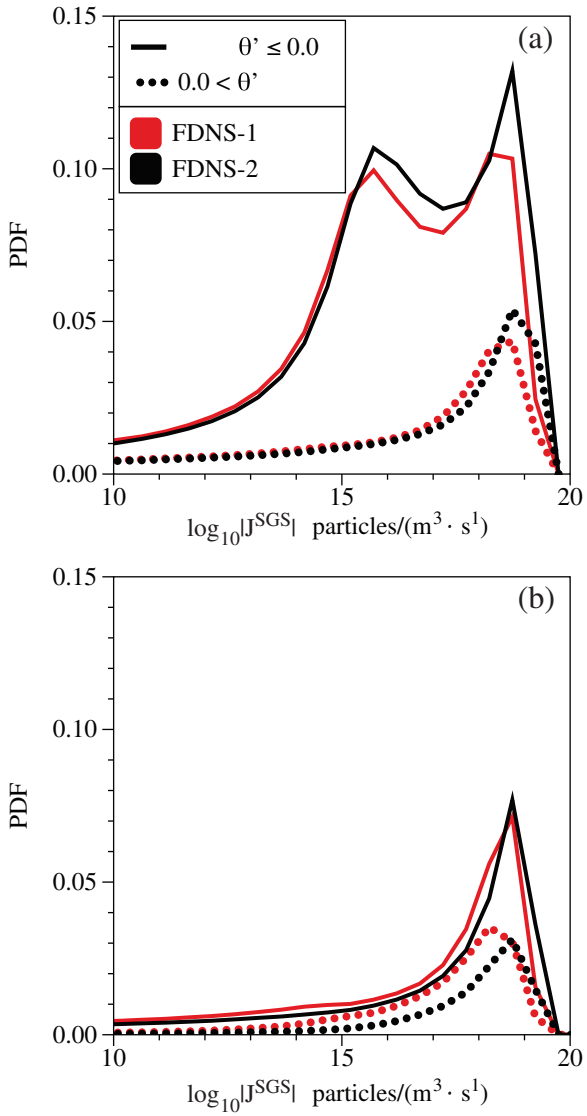

Figure 3.15: Probability density function of subgrid-scale nucleation rate magnitude $|J^{SGS}|$ conditioned on temperature fluctuation θ' at time $t^\star = 80.16$. The red shows $|J_1^{SGS}|$ from the FDNS-1 quantity, while the black shows $|J_2^{SGS}|$ from the FDNS-2 quantity. Panel (a) shows the negative values ($J^{SGS} < 0$) and panel (b) shows the positive values ($J^{SGS} > 0$).

3.7 Nucleating Size distribution

Particle size distributions show the distribution of particles with respect to both their quantity and size. The nucleating size distribution looks only at the distribution of "freshly nucleated" particles. In this study the quantity of particles is shown as a volume fraction of particles V (m^3 particles / m^3 aerosol) and the size of particles is described by the diameter d_p (nm.) The nucleating size distribution is computed via $dV/d\log d_p = 2.3\pi^2 d_p^6 n(v)/12$ where $n(v)$ is the size distribution based on particle number concentration and particle volume, $dN/dv = n(v)$.[1] The distribution is computed from one instance of nucleation rate and critical size and shown in Fig. 3.16. At location $x/D = 1$, shown in Fig. 3.16(a), most particles are nucleating at a size of $d_p = 0.8$ nm. By $x/D = 5$ more and smaller particles are nucleating than at $x/D = 1$, with most forming at a size of $d_p = 0.75$ nm. Further downstream the range of sizes nucleating does not change while the amount of particles nucleating continues to increase. The highest value in the distributions is seen for FDNS-2 at $x/D = 15$ in Fig. 3.16(d) with a peak value of $dV/d\log d_p = 18 \times 10^{-18}$ at $d_p = 0.75$ nm.

Figure (a) shows that at $x/D = 1$ particles are only forming in FDNS-2, suggesting that particles forming sooner in the jet when using only large-scale quantities to compute nucleation (this trend was also seen in Fig. 3.9.) Further downstream FDNS-1 and FDNS-2 over-predict the amount of particles nucleated compared to the DNS, while no difference is seen in the size of particles nucleated. Finally, the figure shows that the over-prediction of particles nucleated decreases with downstream distance in the. For example, at $x/D = 5$ the difference between the peak value in the DNS and FDNS-2 distribution is 430% while at $x/D = 15$ this difference has decreased to 36%. This decrease in the discrepancy of particles nucleated can be attributed to an increasing positive SGS nucleation contribution towards the end of the domain, as seen in Fig. 3.11.

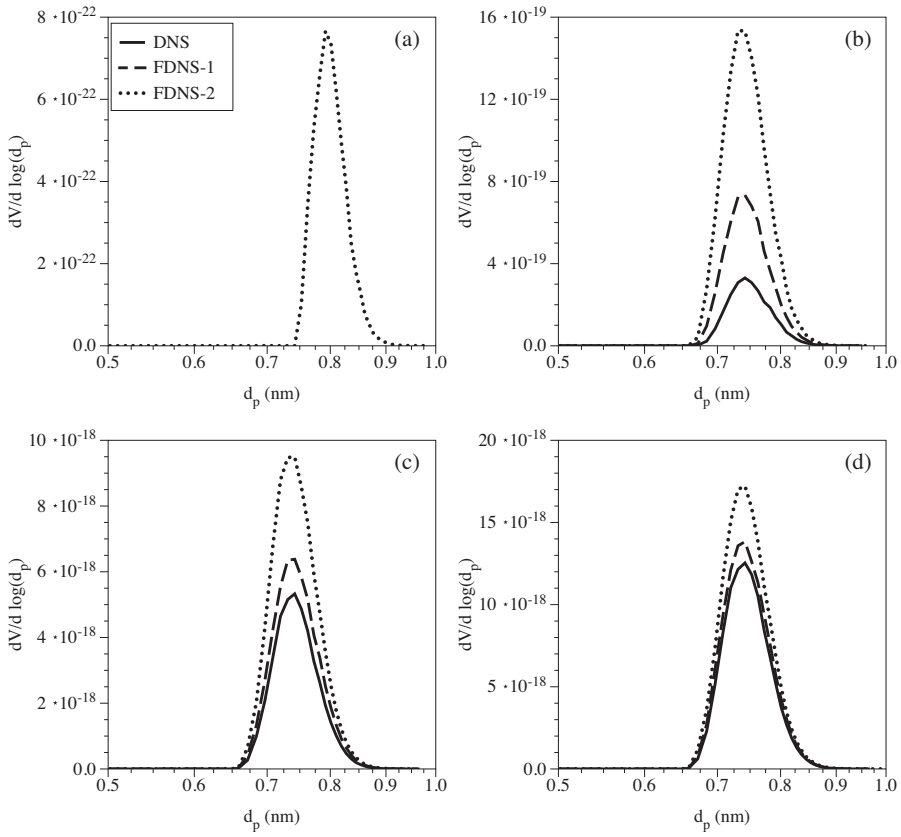

Figure 3.16: Nucleating size distribution at time $t^\star = 80.16$: (a) $x/D = 1$; (b) $x/D = 5$; (c) $x/D = 10$; (d) $x/D = 15$.

3.8 Mean Particle Concentration

The nodal method solves for the particle field as a function of space, time, and size. The results presented will focus on three of the thirteen bins used to approximate the particle field. These are bins 4, 6, and 7 corresponding to particles of size $d_p = 0.90$, 1.43 and 1.81 nm respectively. These sizes are chosen in order to focus separately on the dynamics of particle formation and growth. Formation via nucleation of zinc particles primarily occurs at sub-nanometer critical diameters as can be seen in the nucleating size distributions in Fig. 3.16. Therefore, particles present at $d_p = 0.90$ nm are freshly nucleated. The growth of nucleated particles is captured in the $d_p = 1.43$ and 1.81 nm particle fields. Brownian coagulation from particle-particle collisions is the only growth mechanism considered in this study and results in agglomerates of nucleated particles. Looking at the mean particle field generated from both fully resolved and large- scale quantities allows assessment, in an *a posteriori* manner, of the effects subgrid- scale quantities (or the lack of them) have on the nucleating particle field and the subsequent growth of that field by coagulation.

Cross stream profiles of the time-averaged particle number concentration are show in Fig. 3.17. The profiles show the stream-wise evolution of the mean particle number concentration. In order to show the very large range of concentrations results are presented as the log of number concentration. Figure 3.17(a) shows the concentration of freshly nucleated $d_p = 0.90$ nm particles, $\overline{N_4}$. Initially, particles are only present from nucleation along the interface of the jet and co-flow at $x/D = 1$ and $x/D = 5$. Further downstream particles can be found across the entire jet in increasing concentrations. The general trend is for the particle field calculated from large-scale quantities to over- predict the particle field calculated from exact quantities. This over-prediction decreases with downstream distance. For example, at $x/D = 5$ the FDNS-2 particle field over-predicts the DNS particle field at the peak by 7% based on the logarithm of $\overline{N_4}$. This corresponds to a difference of 2×10^{14} particles/m^3. However, by $x/D = 15$ the FDNS-2 particle field over-predicts the DNS particle field by less than 1% at the peak. This corresponds to a difference of 3×10^{14} particles/m^3. This difference in particle concentration at the peak increasing slightly between $x/D = 5$ and $x/D = 15$ is offset by the order of magnitude increase in total particle concentration between these

two locations.

As particles form via nucleation in the jet, collisions begin to occur leading to growth by coagulation. Brownian coagulation is dependent on the square of particle concentration and therefore in regions of high particle concentration many particle-particle collisions occur. This results in significant growth. As all length scales are resolved in the particle-particle collisions, discrepancies in the concentration of agglomerates between the three simulations are only the result of nucleation discrepancies. Figure 3.17(b) shows the concentration of $d_p = 1.43\ nm$ particles, $\overline{N_6}$. At this size particles begin to appear by $x/D = 5$ from collisions of nucleated particles along the jet/co-flow interface. Further downstream particles appear across the entire jet in increasing concentration, showing that significant growth occurs by coagulation in regions containing the largest concentration of freshly nucleated particles. Similar trends are seen for $d_p = 1.81\ nm$ particles in Fig. 3.17(c). Particles at this size are formed by collisions with both freshly nucleated particles and smaller agglomerates. They are found towards the end of the jet, first appearing in relatively small concentrations at $x/D = 10$. Comparison between the three panels shows that the trend of FDNS-1 and FDNS-2 over-predicting the DNS remains for agglomerates with the over- prediction increasing with particle size. For example, at $x/D = 5$ the percent difference in the peak concentrations between FDNS-2 and DNS for the $d_p = 0.90\ nm$ particle field is 7% while the difference for the $d_p = 1.43\ nm$ particle field is 33%. This suggests that differences in the amount of nucleated particles are compounded when considering growth via coagulation.

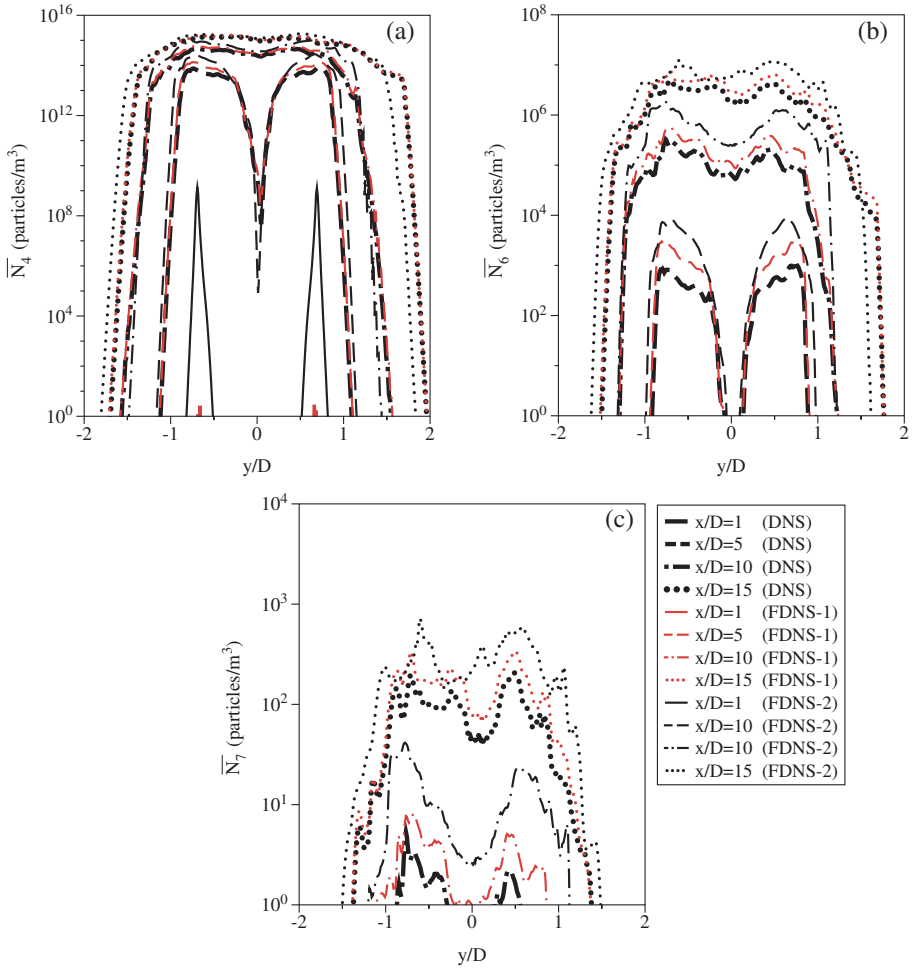

Figure 3.17: Cross-stream profiles of: (a) $d_p = 0.90$nm ($\overline{N_4}$); (b) $d_p = 1.43$nm ($\overline{N_6}$); and (c) $d_p = 1.81$nm ($\overline{N_7}$) particle concentrations.

Chapter 4

Conclusion and Discussion

DNS and hybrid DNS-LESs are performed of zinc nanoparticle formation and growth in turbulent, compressible jets. The DNS uses fully resolved variables and serves as a benchmark for nucleation, while the hybrid DNS-LESs use a variety of fully resolved and large-scale filtered variables to capture and predict the effects of small-scale turbulent features on nucleation. Formation of zinc nanoparticles is by homogeneous nucleation using a size dependent model for the nucleation of metal nanoparticles. Growth of zinc nanoparticles is by Brownian coagulation. Other growth mechanisms, such as condensation, are neglected in this study. A single Reynolds number and initial zinc vapor mass-fraction are used. In all simulations the conservation of mass, momentum, energy, and species are solved with a Navier-Stokes solver in a model-free manner using fully resolved variables. A nodal method is employed to approximate the general dynamic equation and capture the particle field present from size-dependent nucleation and growth by coagulation. Nucleation rate is computed from exact quantities in the DNS while in the hybrid DNS-LESs large-scale filtered quantities are used to compute nucleation rate. Filtering is in the context of LES and removes small-scale features below a prescribed filter width while larger features are preserved. Filtering is performed at two different filter-widths as a real-time operation at each time-step in the simulations. In all simulations the particle growth from coagulation is accounted for by using fully resolved variables. Small-scale turbulent effects are studied in both an *a priori* and *a posteriori* manner.

The results show that cooling from both molecular and convective mixing between

the jet and co-flow leads to a saturated vapor. Nucleation then occurs in regions of saturated vapor. The highest nucleation rates are most prevalent after collapse of the jet core in well mixed regions of the jet. The highest concentrations in the resultant particle field are seen in the post-core collapse regions. Filtering quantities important to nucleation, such as temperature, removes small-scale variations below a prescribed filter-width, while features larger than this filter-width are preserved. Computing nucleation rate from the large-scale filtered temperature, zinc mass-fraction, and density results in more regions of the highest nucleation rate while small pockets or "bursts" of nucleation are removed in the flow. In addition, the onset of particle nucleation occurs sooner (closer to the jet inlet) when based on large-scale variables. These trends increase with filter-width. Looking at the SGS nucleation rate shows the role of unresolved, small-scale interactions in the context of LES. Negative SGS values act to decrease nucleation while positive values act to increase nucleation. Negative values occur first in the jet along the jet/co-flow interface while positive values do not appear in significant quantities until after collapse of the potential core. The predominant effect of the SGS nucleation term is to decrease particle nucleation. Regions of small-scale cooling and dilution are the primary contributors to negative SGS nucleation values. The results suggest that, in the absence SGS models, use of only large- scale variables (as in a LES) results in an over-prediction in the number of particles nucleated. This over-prediction is expected to be largest in laminar and transitional flow regimes and decreasing as transition to turbulence occurs. Using a larger filter width increases the over-prediction of nucleated particles. The trends seen when the filter-width is increased are useful as they show expectations for even larger filter-widths that may be used in practical LES studies. No significant discrepancies in the size of nucleated particles is seen when using large- scale variables. Differences in the nucleating particle field from the use of large-scale variables are compounded when considering growth by coagulation. These results suggest that in LES the largest over-predictions in the nucleating particle field are expected in laminar and transition flow regimes, while the over-prediction is expected to be relatively small in fully turbulent flow regimes.

DNS is possible for simple flows, such as the round jet this study. However, it quickly becomes impossible for flows of practical, engineering interest where complex geometries, thermochemistry, and fluid-particle/particle-particle interactions may exist

simultaneously. For these engineering flows LES and RANS are the practical alternatives. LES is attractive as it captures large-scale, time-dependent flow features not possible in a RANS but has a speed up factor of over 1000 when compared to DNS. [12] However, there is a need for SGS models as this and other studies have shown that the unresolved small-scale terms are still important for accurately predicting particle formation and growth in LES.[11, 46] This work shows that discrepancies in the nucleating particle field, from the lack of SGS models, could be significant in subsequent particle growth by coagulation. Growth by condensation was not investigated in this study. However, condensation could be a significant growth mechanism and should be considered in future studies where accurate particle growth in a nucleating system is desired. [8] While this study shows the effects of the unresolved small-scale terms in a metal nanoparticle nucleating system, understanding of the SGS effects for many more nucleating systems is needed for the widespread adoption of LES to predict particle formation and growth in complex, turbulent flows.

References

[1] K. S. Friedlander. *Smoke, Dust and Haze: Fundamentals of Aerosol Dynamics.* Oxford University Press, New York, NY, 2000.

[2] T. T. Kodas, A. Sood, and S. E. Pratsinis. Submicron alumina powder production by a turbulent flow aerosol process. *Powder Technology*, 50:47–53, October 1986.

[3] E. G. Moody and L. R. Collins. Effect of mixing on the nucleation and growth of titania particles. *Aerosol Sci. Technol.*, 37(5):403–424, 2003.

[4] S. E. Pratsinis and S. Vemury. Particle formation in gases: A review. *Powder Technology*, 88(3):267–273, 1996.

[5] P. P. Wegener and A. A. Pouring. Experiments on condensation of water vapor by homogeneous nucleation in nozzles. *Phys. Fluids.*, 7:352–361, 1964.

[6] D. Kashchiev. On the relation between nucleation work, nucleus size, and nucleation rate. *J. Chem. Phys.*, 76(10):5098–5102, May 1982.

[7] A. Garmory and E. Mastorakos. Aerosol nucleation and growth in a turbulent jet using the stochastic fields method. *Chem. Eng. Sci.*, 63:4078–4089, 2008.

[8] T. Lesniewski and S. K. Friendlander. Particle nucleation and growth in a free turbulent jet. *Proc. R. Soc. Lond. A*, 454:2477–2504, 1998.

[9] C. Housiadas, Y. Drossinos, and M. Lazaridis. Effect of small-scale turbulent fluctuations on rates of particle formation. *J. Aerosol Sci.*, 35(5):545–559, 2004.

[10] H. Tammet and M. Kulmala. Simulation tool for atmospheric aerosol nucleation bursts. *J. Aerosol Sci.*, 36:173–196, 2005.

[11] S. Das and S. C. Garrick. The effects of turbulence on nanoparticle growth in turbulent reacting jets. *Phys. Fluids*, 22, October 2010.

[12] J. Loeffler, S. Das, and S. C. Garrick. Large eddy simulation of titanium dioxide nanoparticle formation and growth in turbulent jets. *Aerosol Sci. and Technol.*, 2011. in press.

[13] S. C. Garrick. Large eddy simulations of a turbulent reacting mixing layer. AIAA Paper 95-0010, 1995.

[14] P. J. Colucci, F. A. Jaberi, P. Givi, and S. B. Pope. Filtered density function for large eddy simulation of turbulent reacting flows. *Phys. Fluids*, 10(2):499–515, 1998.

[15] F. A. Jaberi, P. J. Colucci, S. James, P. Givi, and S. B. Pope. Filtered mass density function for large eddy simulation of turbulent reacting flows. *J. Fluid Mech.*, 401, December 1999.

[16] J. C. Oefelein, R. W. Schefer, and R. S. Barlow. Toward validation of large eddy simulation for turbulent combustion. *AIAA*, 44(3):418–433, March 2006.

[17] G. Y. Di Veroli and S. Rigopoulos. Modeling of aerosol formation in a turbulent jet with the transported population balance equation-probability density function approach. *Phys. Fluids*, 23:043305, 2011.

[18] S. C. Garrick, F. A. Jaberi, and P. Givi. Large eddy simulation of scalar transport in a turbulent jet flow. In D. Knight and L. Sakell, editors, *Recent Advances in DNS and LES*, volume 54 of *Fluid Mechanics and its Applications*, pages 155–166. Kluwer Academic Publishers, The Netherlands, 1999.

[19] S. C. Garrick, K. E. J. Lehtinen, and M. R. Zachariah. Nanoparticle coagulation via a Navier–Stokes/nodal methodology: Evolution of the particle field. *J. Aerosol Sci.*, 37(5):555–576, 2006.

[20] F. Gelbard and J. H. Seinfeld. Simulation of multicomponent aerosol dynamics. *J. Colloid Interface Sci.*, 78:485–501, 1980.

[21] F. Gelbard, Y. Tambour, and J. H. Seinfeld. Sectional representations for simulating aerosol dynamics. *J. Colloid Interface Sci.*, 76:541–556, 1980.

[22] P. Biswas, C. Y. Wu, M. R. Zachariah, and B. McMillin. Characterization of iron oxide-silica nanocomposites in flames: Part II: Comparison of discrete- sectional model predictions to experimental data. *J. Mat. Res.*, 12:714–723, 1997.

[23] K. E. J. Lehtinen and M. R. Zachariah. Energy accumulation in nanoparticle collision and coalescence processes. *J. Aerosol Sci.*, 33:357–368, 2002.

[24] S. Modem, S. C. Garrick, M. R. Zachariah, and K. E. J. Lehtinen. Direct numerical simulation of nanoparticle coagulation in a temporal mixing layer. In *Proceedings of the 29th Symp. (Int.) on Combustion*, pages 1071–1077. The Combustion Institute, Pittsburgh, PA, 2002.

[25] S. Modem and S. C. Garrick. Nanoparticle coagulation in a temporal mixing layer: Mean and size-selected images. *J. Visualization*, 6(3):333–342, 2003.

[26] B. Guo and I. M. Kennedy. The speciation and morphology of chromium oxide nanoparticles in a diffusion flame. *Aerosol Sci. Technol.*, 38(5):424–436, May 2004.

[27] G. W. Mulholland, R. J. Samson, R. D. Mountain, and M. H. Ernst. Cluster size distribution for free-molecular agglomeration. *Energy & Fuels*, 2:481–486, 1988.

[28] S. L. Girshick and C. Chiu. Kinetic nucleation theory: A new expression for the rate of homogeneous nucleation from an ideal supersaturated vapor. *J. Chem. Phys.*, 93(2):1273–1277, 1990.

[29] A. A. Onischuk, P. A. Purtov, A. M. Baklanov, V. V. Karasev, and S. V. Vosel. Evaluation of surface tension and tolman length as a function of droplet radius from experimental nucleation rate and supersaturation ratio: Metal vapor homogeneous nucleation. *J. Chem. Phys.*, 124(014506), 2006.

[30] J. Liu and S. C. Garrick. Comment on "Evaluation of surface tension and tolman length as a function of droplet radius from experimental nucleation rate and supersaturation ratio: Metal vapor homogeneous nucleation". *J. Chem. Phys.*, 133(4), 2010.

[31] H. Reiss, W. K. Kegel, and J. L. Katz. Role of the model dependent translational volume scale in the classical theory of nucleation. *J. Phys. Chem. A*, 102:8548–8555, 1998.

[32] B. E. Launder, G. J. Reece, and W. Rodi. Progress in the development of a Reynolds-stress turbulence closure. *J. Fluid Mech.*, 68:537–566, 1975.

[33] W. C. Reynolds. Computation of turbulent flows. *Annu. Rev. Fluid Mech.*, 8:183–208, 1976.

[34] A. A. Aldama. Filtering techniques for turbulent flow simulations. volume 49 of *Lecture Notes in Engineering*. Springer-Verlag, New York, NY, 1990.

[35] S. B. Pope. *Turbulent Flows*. Cambridge University Press, Cambridge, UK, 2000.

[36] P. E. DesJardin and S. H. Frankel. Large eddy simulation of a nonpremixed reacting jet: Application and assessment of subgrid-scale combustion models. *Phys. Fluids*, 10(9):2298–2313, 1998.

[37] C. J. Rutland and J. H. Ferziger. Simulations of Flame-Vortex interactions. *Combust. Flame*, 84:343–360, 1991.

[38] P. P. Wegener and K. R. Sreenivasan. The effect of cooling rate on binary nucleation. *Applied Scientific Research*, 37:183–194, 1981.

[39] L.S. Bartell. Tolman's length, surface curvature, compressibility effects, and the free energy of drops. *J. Phys. Chem. B*, 105:11615–11618, 2001.

[40] R. W. MacCormack. The effect of viscosity in hypervelocity impact catering. AIAA Paper 69-354, 1969.

[41] C. A. Kennedy and M. H. Carpenter. Several new numerical methods for compressible shear-layer simulations. *Appl. Num. Math.*, 14:397–433, 1994.

[42] A Okubo. Horizontal dispersion of floatable trajectories in the vicinity of velocity singularities such as convergencies. *Deep Sea. Res.*, 17:445–454, 1970.

[43] J Weiss. The dynamics of enstrophy transfer in 2-dimensional hydrodynamics. *Physica D*, 48:273–294, 1991.

[44] G. Haller and G. Yuan. Lagrangian coherent structures and mixing in two-dimensional turbulence. *Physica D*, 147:352–370, 2000.

[45] R.L. Panton. *Incompressible Flow*. John Wiley {& sons, New York, USA, 1984.

[46] S. C. Garrick. Effects of turbulent fluctuations on nanoparticle coagulation in shear flows. *Aerosol Sci. and Technol.*, 45:1271–1285, 2011.

[47] A. V. Oppenheim and R. W. Schafer. *Discrete-Time Signal Processing*. Prentice Hall, Englewood Cliffs, NJ, 1989.

[48] J. M. Ottino. *The Kinematics of Mixing: Stretching, Chaos, and Transport*. Cambridge University Press, Cambridge, UK, 1989.

[49] Y. Zhou, M. Hossain, and G. Vahala. A critical look at the use of filters in large eddy simulation. *Physics Letters A*, 139(7):330–332, 1989.